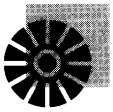

Contributed Paper

Impurity Transport and Its Application to Ion Temperature Measurement in JT-60U Divertor Plasmas

NAKANO Tomohide, KUBO Hirotaka, ASAKURA Nobuyuki, SHIMIZU Katsuhiro and HIGASHIJIMA Satoru

Naka Fusion Research Establishment, Japan Atomic Energy Research Institute, Naka, Ibaraki 311-0193, Japan

(Recieced 11 June 2004 / Accepted 5 April 2004)

The ratio of population densities of C^{3+} excited levels, $C^{3+}(3p^2P_{3/2})$, $C^{3+}(n = 6)$, and $C^{3+}(n = 7)$, indicates that $C^{3+}(n = 7)$ is predominantly excited by electron collision with the ground state of C^{3+} in attached plasmas. Hence, Doppler broadening of the C IV ($n = 6 - 7$) spectral line provides C^{3+} temperature. Regression analysis of the spectrum results in two C^{3+} temperature components. The higher C^{3+} temperature ranges from 50 eV to 150 eV, the lower around 20 eV. From the results of the analyses with plasma and impurity transport codes and a collisional-radiative model, the higher and the lower C^{3+} temperature correspond to the C^{3+} temperature of the common flux (divertor) plasma and of the private plasma, respectively. In the inner divertor, C^{3+} temperature is close to D^+ temperature, and the C IV spectral line is predominantly emitted around the inner divertor leg. Therefore, it is concluded that D^+ temperature around the inner divertor leg can be measured from the C IV spectral line. On the contrary, it is found difficult to measure the D^+ temperature in the outer divertor.

Keywords:

impurity transport, ion temperature, spectroscopy, atomic process, divertor, tokamak, JT-60U

1. Introduction

In tokamak divertors, hydrogen ion temperature in the peripheral region is one of the key parameters to understand plasma and impurity behaviors, and, consequently, is information essential to controlling divertor plasmas. However, because the ion has no line emission, it is difficult to measure the ion temperature directly by spectroscopy. Plasma and impurity behaviors have often been discussed without inclusion of measured ion temperature. Relative to advanced studies of the plasma and impurity behaviors, the importance of ion temperature measurement is increasing.

The heat and the particles exhausted from a main plasma are generally transported along magnetic field lines. The particle flow direction is determined by the pressure balance [1], and it is usually from the edge region of the main plasma toward the divertor because the divertor works as a particle sink. The ion transported to the divertor collides with its target plates, resulting in impurity generation. Both the physical [2] and the chemical [3] sputtering yields increase with increasing impact energy. Some of the sputtered impurities are shielded by the divertor plasma while others are transported upstream to the main plasma by thermal force [4]. During the transport, these impurities obtain kinetic energy by ion collision. This is also the case for a fusion byproduct, helium atom. The elastic collision with ion scatters helium atom, and enhances penetration of helium atom to the main plasma as well as exhaust through the pumping slots [5]. Hence, the ion behavior in the divertor plasmas is of significant importance to determine the divertor performance, that is, the controllability of heat, particles and impurity. However, the ion behaviors have often been discussed with the ion temperature under the assumption of an ion temperature equal to the electron temperature or invoked from the pressure balance [6]. The ion temperature should be verified by experimental measurements.

Direct particle measurement such as ion-sensitive probe measurement [7,8] is one method by which to measure the ion temperature. But the ion temperature profile only along the probe chord is obtained, and it is difficult to measure the time evolution of the ion temperature because the measurement duration is often limited by the heat and particle fluxes of the plasma. In addition, in some cases, the change of the plasma caused by the probe insertion cannot be neglected. Although direct and local measurement is difficult, there are advantages in optical spectroscopy. In particular, visible spectroscopy has advantages in spatial-resolved and absolute-intensity measurements. In the case that optical fibers are used as object optics, viewing chords can be selected by changing the arrangement of the optical fibers guided to a spectrometer. The absolute-intensity measurement provides quantitative analysis, that is, absolute (line-integral) density comparison with analytic code predictions, led to a

author's e-mail: nakanot@fusion.naka.jaeri.go.jp

This article is based on the invited talk at the 19th JSPF Annual Meeting (2002, Inuyama).

comprehensive understanding of the plasma and impurity behaviors.

For measuring the ion temperature from a carbon spectral line, a highly charged carbon ion is preferred because the temperature relaxation time is inversely proportional to the square of the carbon ion charge. From this point of view, there are preferred spectral lines, i.e., C VI ($n = 7 - 8 : \lambda \sim 529.1$ nm) [9] and C V ($2s^3S - 2p^3P : \lambda \sim 227.2$ nm). However, both lines are not available in JT-60U divertor plasmas. The intensity of the C VI spectral line is too weak, and the wavelength of the C V spectral line is below the wavelength cutoff (~ 350 nm in JT-60U) due to low transmission of the long optical fiber between JT-60U and the diagnostic room. On the contrary, the intensity of C IV ($n = 6 - 7 : \lambda \sim 772.6$ nm) is sufficient. In addition, this spectral line has another advantage in the ion temperature measurement. If neutral hydrogen density is high as it is in detached divertor plasmas, the dominant process to populate the $n = 7$ level of C^{3+} changes from the electron impact excitation of the ground-state of C^{3+} to the charge exchange recombination between $D^0(n = 2)$ and C^{4+}. In this case, this spectral line reflects the C^{4+} temperature. For these reasons, the C IV ($n = 6 - 7$) spectral line was chosen in the present work. The analysis was done with attention to the temperature relaxation time between ion and carbon ions as well as to the elementary processes of C^{3+} and C^{4+}. The present work is focused on an attached divertor plasma. Brief description of a detached plasma is included.

2. Experimental

Figure 1 (a) shows a schematic view of the poloidal cross-section of JT-60U and a spectroscopic diagnostic system for a divertor plasma. A w-shaped divertor, composed of baffles, divertor plates, and a dome, is positioned at the bottom of the vacuum vessel. Carbon fiber composite (CFC) materials are used for the divertor plates and some of the dome plates, and isotropic graphite materials are used for the other dome plates and plates for the main chamber.

The spectroscopic diagnostic system consists of an object optics, two parallel arrays of sixty optical fibers, and three spectrometers. The object optics covers the divertor region with a spatial resolution of ~ 1.2 cm with the sixty optical fibers, as shown in Fig. 1 (b). Emission from the divertor plasma is collimated with two lenses. The π light of the emission, a polarization component parallel to the toroidal magnetic field, is transmitted through a linear polarizer placed between the lenses and focused onto the arrays of the optical fibers. Then the light is transmitted to a diagnostic room through the optical fibers (core diameter : 200 μm). In the diagnostic room, ten, sixteen, and sixty optical fibers are guided to a high resolution spectrometer, a low resolution spectrometer, and an interference filter optics, respectively.

The high resolution spectrometer [10] observes ten spectra of C IV ($n = 6 - 7 : \lambda \sim 772.6$ nm) simultaneously. This spectrometer is built in the Littrow mounting with an echelle grating. The Littrow lens (focal length : 1.2 m, diameter : 100 mm) is used for suppression of astigmatic images of the optical fibers, the echelle grating (79 grooves / mm, height : 102 mm, width : 254 mm, blazing angle : 74°) for high wavelength resolution at high spectral orders. The C IV ($n = 6 - 7$) spectral lines are observed at the 32nd spectral order in the case that the angle of the echelle grating is set at the highest diffraction efficiency. The dispersed light is detected with a charge coupled device (CCD) camera having an image-intensifier (quantum efficiency : ~ 40%), which has 512 × 512 pixels with an effective size of 24 × 24 μm. The dispersion and the absolute wavelength were determined from two Ar I lines (wavelength : 772.37600 and 772.42066 nm ± 0.000053 nm [11]) by means of a spectral calibration lamp. The measured dispersion is 0.00182 nm / pixel with an estimated error of 0.00001 nm, and the constant dispersion is assumed to determine the absolute wavelength. The instrumental function was measured by means of a He-Ne laser. The full width at half maximum (FWHM) of the measured instrumental function is ~ 0.0062 nm (~ 3.4 pixel) at a slit width of 80 μm, while the FWHM of the Doppler broadening ranges between 0.06 and 0.2 nm. Because of the high wavelength resolution, this spectrometer can provide spectra for Doppler profile analysis. In addition, the line-integral population density of the $n = 7$ level is derived from the measured brightness, which is proportional to the product of spontaneous transition probability and population density of the upper level of the transition.

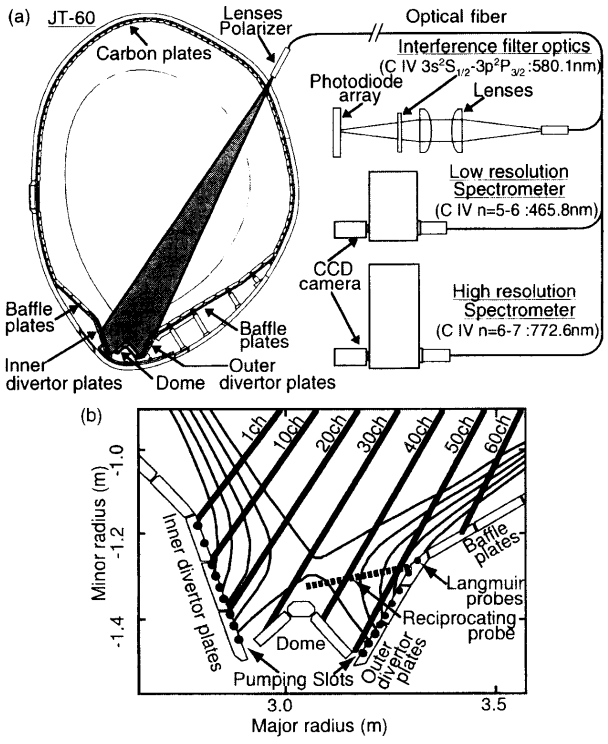

Fig. 1 (a) Schematic view of the poloidal cross-section of JT-60U and spectroscopic diagnostic systems. (b) Expanded view around the w-shaped divertor. Plasma configuration, viewing chords for spectroscopic measurements, a reciprocating probe chord, and locations of Langmuir probes are shown.

Figure 2 (a) shows a spectrum of C IV (n = 6 – 7) observed with the high resolution spectrometer. The spectrum is composed of three spectral lines, $6f - 7g$, $6g - 7h$, and $6h - 7i$. For these levels, the energy difference due to the fine-structure splitting is so small that each of these lines cannot be resolved to spectral lines corresponding to transitions between total angular momentum quantum numbers. The removal of the σ components, split due to the Zeeman effect, contributes to reducing errors of regression analysis on the spectral profile. A Gaussian function may be applicable to the regression analysis because the Doppler broadening is considered to determine the spectral profile. Actually, as shown in Fig. 2 (a), two Gaussians for each line, six Gaussians in total, were necessary to reproduce the tails of the spectrum. This double spectral profile suggests that both cold plasma and hot plasma, investigated later, exist along the viewing chord. It should be noted that three Gaussians do not significantly reduce the residual of the spectral profile and the regression curve, and that the instrumental width is too narrow to affect the spectral profile.

The wavelengths of the three spectral lines determined in the present work are shown in Table 1. Because the viewing chord is almost perpendicular to the magnetic field line, the plasma flow across the magnetic filed line could cause the Doppler shift of the spectral lines. In fact, the wavelengths determined from all the ten spectra agree within the estimated error. This result supports that the plasma flow across the magnetic filed line is not very significant anywhere in the divertor. On the assumption that the Doppler shift is negligible, the wavelengths calculated from the energy levels given in [12] are in agreement within the estimated error (~ 0.06 nm). But the wavelengths are systematically longer by ~ 0.01 nm than those determined in the present work. In contrast, the wavelength calculated by the polarization formula [13] are systematically shorter by ~ 0.005 nm. The agreement with the present work is better, though the difference remains larger than the estimated error.

As shown in Fig. 2 (a), the intensities of the three spectral lines appear proportional to gA, where g is a statistical weight of the upper level of the transition, and A is a spontaneous transition probability. In fact, the population densities of the n = 7 level are distributed among azimuthal quantum numbers (l-levels) having the ratio of the statistical weight. From the result of simple calculation, which considers spontaneous transition from l-levels of n = 7 to l-levels of $n \leq 7$, electron and deuteron impact excitation/de-excitation between l-levels of n = 7, it is concluded that this statistical population-distribution is ascribed to the deuteron impact on $C^{3+}(n = 7)$. The result calculated at an electron temperature and an electron density of 50 eV and 1.0×10^{19} m^{-3} indicates that more than 98% of the population flows between high l-levels, i.e., $7f$, $7g$, $7h$ and $7i$, is due to the deuteron impact excitation/de-excitation, and that the populating flow to an l-level is equal to the de-populating flow from the l-level by the principle of detailed balance. As a result, the population densities of these l-levels distribute along the ratio of the

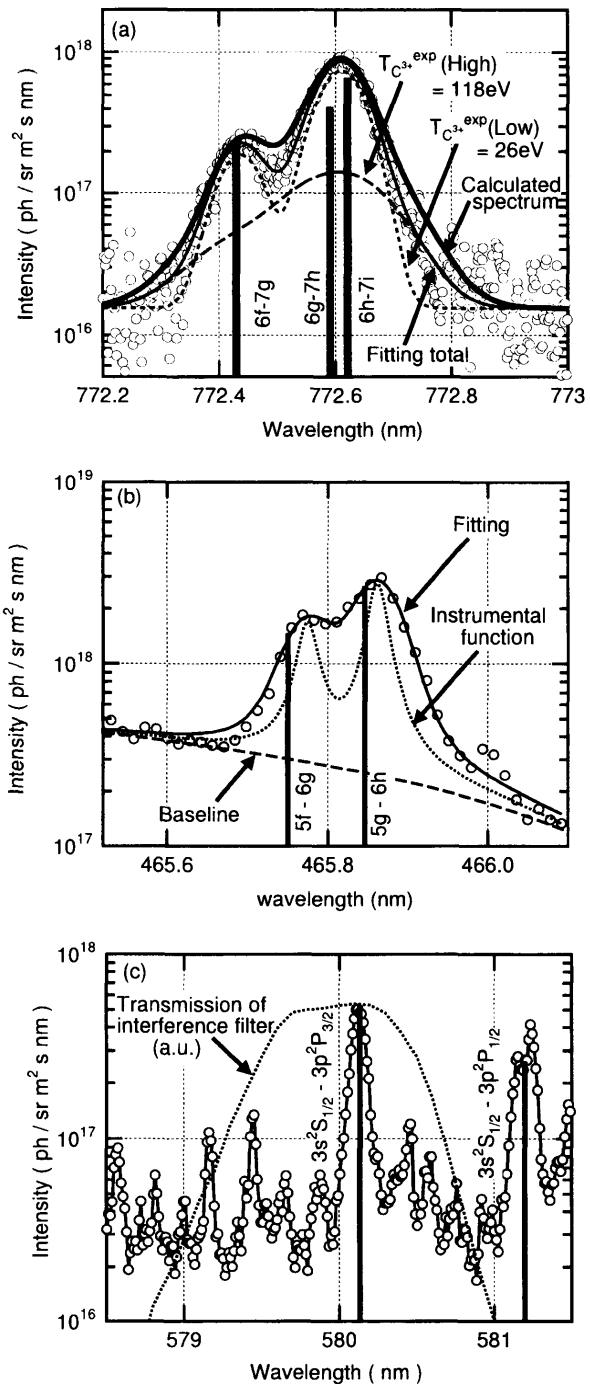

Fig. 2 Observed spectra (π component) of (a) C IV (n = 6 – 7), (b) C IV (n = 5 – 6) and (c) C IV ($3s^2S_{1/2} - 3p^2P_{3/2,\ 1/2}$), shown by open circles. The location and the length of the vertical lines show, respectively, the wavelength calculated by the polarization formula [13] and normalized gA. In (a), the solid thin curve shows the regression curve, which is resolved into two curves, a high temperature ($T_{C^{3+}}^{exp}$(High)) and a low temperature ($T_{C^{3+}}^{exp}$(Low)) component, shown by the dashed and the dotted curve, respectively. The solid thick curve shows the spectrum calculated by the transport codes and the collisional-radiative model. In (b), the dotted and the solid thin curve show the instrumental function and the regression curve, respectively. The baseline shown by the dashed curve is used as the tail of an adjacent spectral line, C III ($3s^3S - 3p^3P$: λ ~ 464.7 nm). In (c), the relative transmission of the interference filter is shown by the dotted curve.

Table 1 Wavelengths of C IV (n = 6 – 7) and C IV (n = 5 – 6) determined in the present work, deduced from the experimental energy levels [12] and calculated by the polarization formula [13]. Estimated experimental errors are also shown.

Transition	Present work	estimated error	Experiment [12]	estimated error	Calculation [13]
6*f* – 7*g*	772.438 nm	~ 0.001 nm	772.45 nm	~ 0.06 nm	772.430 nm
6*g* – 7*g*	772.595 nm		772.60 nm		772.591 nm
6*g* – 7*i*	772.626 nm		772.64 nm		772.621 nm
5*f* – 6*g*	465.775 nm	~ 0.002 nm	465.71 nm	~ 0.02 nm	465.751 nm
5*g* – 6*g*	465.862 nm		465.89 nm		465.846 nm

statistical weight.

The low resolution spectrometer [14] observes sixteen spectra of C IV (n = 5 – 6) around 465.8 nm, simultaneously. This spectrometer has a 0.5 m Czerny-Turner-type optics with a 2400 grooves/mm grating, and an image-intensified CCD camera having 512 × 512 pixels covers a spectral band of ~ 7.2 nm. Figure 2 (b) shows the observed spectrum, which is composed of two spectral lines corresponding to the 5*f* – 6*g* and 5*g* – 6*h* transitions, respectively. The FWHM of the instrumental function at an entrance slit width of 30 μm is ~ 0.03 nm, and this value, compared with the FWHM of the Doppler broadening (≥ 0.06 nm), is not narrow enough to analyze the spectral profile. The observed spectrum is not used for the temperature measurement but for the brightness measurement of the spectral line, which is converted to the line-integral population density of the n = 6 level. As shown in Table 1, the wavelengths determined in the present work are in better agreement with those calculated by the polarization formula [13] than with those deduced from the energy levels [12]. The wavelength differences between the present work and the previous reports are larger than those of C IV (n = 6 – 7). This larger difference is not due to the Doppler shift, considering that the Doppler shift of C IV (n = 5 – 6) cannot be different from that of C IV (n = 6 – 7). The ratio of population densities of the 6*g* and 6*h* levels is close to the ratio of the statistical weight, similar to the case for the ratio of 7*g*, 7*h*, and 7*i* levels, due to the principle of detailed balance, described above for the n = 7 levels.

The interference filter optics with a photo diode array [15] measures the brightness of the C IV ($3s^2S_{1/2} - 3p^2P_{3/2}$) spectral line at a wavelength of 580.1 nm. As shown in Fig. 2 (c), the center wavelength of the transmission band and the FWHM of the interference filter are ~ 580.0 nm and ~ 1.0 nm, respectively. The measured brightness is converted to the line-integral population density of the $3p^2P_{3/2}$ level.

For the present measurement, discharge conditions were as follows: a plasma current of 1.5 MA, a toroidal field of 3.5 T, a neutral beam heating power of 4.3 MW, and a line-averaged electron density of the core plasma of 1.8×10^{19} m^{-3}. This discharge was an L-mode plasma with both the inner and the outer divertor attached to the divertor plates. Electron temperature and density measured by Langmuir probes on the divertor plates are shown in Fig. 3. Around the strike point on the inner divertor plate, the electron temperature and density were 15 eV and 2.3×10^{19} m^{-3}, respectively. Around the strike point on the outer divertor

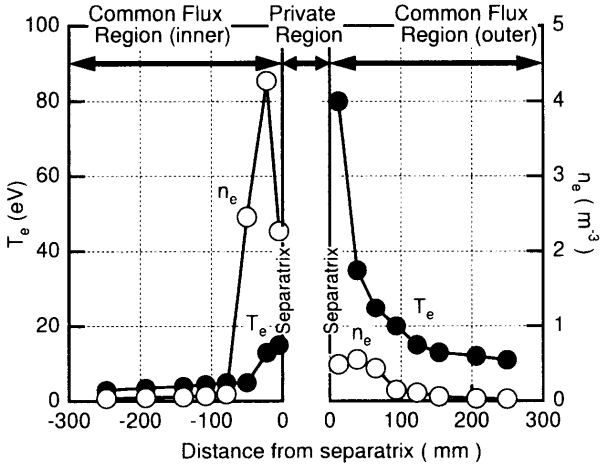

Fig. 3 Electron temperature (T_e) and density (n_e) on the divertor plates measured by Langmuir probes. Closed and open circles show the electron temperature and density, respectively.

plate, the electron temperature and density were 80 eV and 0.5×10^{19} m^{-3}, respectively. From the above divertor plasma, the three spectral lines, C IV ($3s^2S_{1/2} - 3p^2P_{3/2}$), C IV ($n$ = 5 – 6), and C IV (n = 6 – 7) were observed simultaneously. The spectroscopic signals were integrated for 0.3 s in order to reduce statistical errors. The reciprocating probe, whose chord is shown in Fig. 1 (b) [16], measured the electron temperature and density.

3. Analysis Method

In order to analyze the spectroscopic data, the following steps are taken. First, a plasma transport code determines the two-dimensional distribution of plasma and neutral parameters, i.e., the temperatures and densities of electron, ion, and neutral deuterium. Second, for the background plasma calculated in the first step, an impurity transport code determines the two-dimensional distribution of the impurity parameters, i.e., the temperatures and densities of neutral carbon and carbon ions. Third, in each cell used in the above calculations, population densities of the excited levels of C^{3+} are determined by a collisional-radiative model. Fourth, the spectrum in the cell is synthesized using emission intensity and spectral width. Finally, the observed spectrum is compared with the synthesized spectrum summed up along the viewing chord. In this section, descriptions on the two transport codes and the collisional-radiative model are given.

3.1 Plasma and impurity transport codes

Two-dimensional distribution of plasma, neutrals, and impurity parameters is determined by two transport codes, i.e., the Simple Diverter code [17] and the IMPMC code [4]. Figure 4 shows the mesh used for the present simulation. Hereafter, the plasma region is defined as shown in Fig. 4; the peripheral plasma is divided into two regions, the common flux plasma and the private plasma. Further, the common flux plasma is divided into the scrape-off-layer (SOL) plasma and the divertor plasma.

The Simple Divertor code determines the spatial distribution of the temperatures and densities of electron, ion, and neutral deuterium. This code needs, as boundary conditions, electron temperature, electron density, and ion temperature on the divertor plates. For the present study, the electron temperature and density measured by Langmuir probes, shown in Fig. 3, were used as the boundary conditions, and the ion temperature was assumed to be equal to the electron temperature. Next, this code solves fluid equations numerically along magnetic field lines from the divertor plasma to the SOL plasma for the common flux plasma. This code cannot solve fluid equations for the private plasma. In the calculation, the cross field transport of plasma is neglected. This code also simulates neutral particle transport two-dimensionally using Monte Carlo techniques. The interaction between the plasma and the neutrals is solved self-consistently and iteratively until the plasma parameters converge, resulting in steady-state solution.

Next, the IMPMC code determines the temperatures and densities of neutral carbon and carbon ions. This code simulates carbon generation, ionization/recombination, and transport two-dimensionally using Monte Carlo techniques.

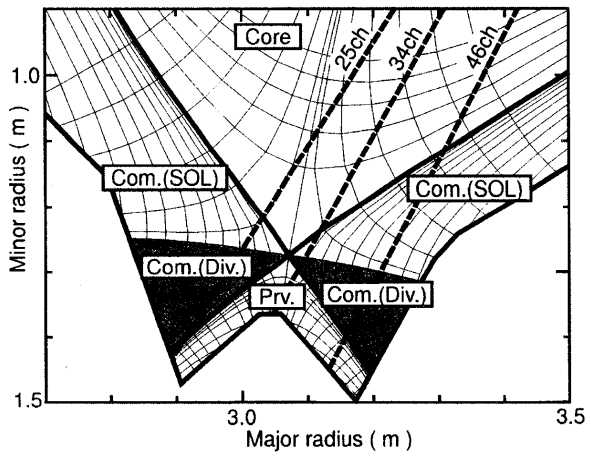

Fig. 4 The mesh used for the present simulation. Thick solid line shows plasma separatrix. Dashed lines show spectroscopic viewing chords for the inner divertor, the X-point, and the outer divertor. For these viewing chords, detailed comparison of the simulation and the measurement is given. The common flux plasma (denoted by Com.) consists of scrape-off-layer plasma (denoted by SOL) and divertor plasma (shaded area and denoted by Div.). The private plasma (denoted by Prv.) is a plasma between the separatrix and the dome.

Carbon atom and methane are generated by physical and chemical sputtering, respectively. The carbon atom, the methane and its radicals travel at constant velocities until they ionize. Parallel motion of the ions along magnetic field lines by Coulomb scattering and cross-field diffusion are simulated. Atomic processes of ionization, recombination, and charge exchange recombination are considered.

3.2 Collisional-radiative model

A collisional-radiative model has been developed to determine the population density of the excited level of C^{3+}, and then to predict the emission intensityof the C IV spectral lines.

3.2.1 Rate equation and solution

The temporal development of the population density of C^{3+}, $n_{C^{3+}(p)}$, is expressed as the differential equation,

$$\begin{aligned}\frac{\mathrm{d}}{\mathrm{d}t} n_{C^{3+}(p)} = & -\left\{\sum_{q<p} A(p,q) + \sum_{q\neq p} C(p,q) n_e + S(p) n_e\right\} n(p) \\ & + \left\{\sum_{q>p} A(q,p) + \sum_{q\neq p} C(q,p) n_e\right\} n(q) \\ & + \left\{\alpha(p) n_e + \beta(p) + \gamma(p)\right\} n_{C^{4+}} n_e \\ & + \sum_{n=1,2} q^{CX}(n,p) n_{D^0(n)} n_{C^{4+}}, \end{aligned} \quad (1)$$

which is coupled with similar equations for other levels. Here p and q stand for the level that is determined by a principal quantum number n or combination of n and an azimuthal quantum number l. In eq.(1), $q < p$ means that level q lies energetically lower than level p. The spontaneous transition probability from level p to level q is denoted by $A(p, q)$. The rate coefficients for electron impact excitation if $p < q$ (de-excitation if $p > q$) and ionization are denoted by $C(p, q)$ and $S(p)$, respectively. The rate coefficients for three-body, radiative and di-electronic recombination are denoted by $\alpha(p)$, $\beta(p)$, and $\gamma(p)$, respectively. These rate coefficients are a function of electron temperature T_e. In eq.(1), n_e and $n_{C^{4+}}$ denote electron density and C^{4+} density, respectively.

We have extended the collisional-radiative model so that it can handle charge exchange recombination processes from D^0 to C^{4+}, which play an important role to determine the ratio of C^{3+} to C^{4+} [4,18,19]. Not only the ground-state deuterium, $D^0(n = 1)$, but also the excited-state deuterium, $D^0(n = 2)$, reacts with C^{4+}, resulting in a predominant increase of the population densities of $C^{3+}(n = 3)$ and $C^{3+}(n = 6)$, respectively. This is because the level energies of $C^{3+}(n = 3)$ and $C^{3+}(n = 6)$ from the ionization potential are close to those of $D^0(n = 1)$ and $D^0(n = 2)$, respectively. The charge exchange recombination cross-section from $D^0(n = 2)$ to C^{4+} is larger than that from $D^0(n = 1)$ to C^{4+} by a factor of > 10. Here, the charge exchange recombination processes from $D^0(n \geq 3)$ to C^{4+} are ignored in our collisional-radiative model because they do not significantly affect the population densities of $C^{3+}(n \geq 7)$.

On the right side of eq.(1), the term $q^{CX}(n, p)\, n_{D^0(n)} n_{C^{4+}}$ (n = 1, 2), where $q^{CX}(n, p)$ is the rate coefficient for the charge exchange recombination from $D^0(n)$ to C^{4+}, which populates $C^{3+}(p)$, is added. Here, $n_{D^0(n)}$ is the population density of $D^0(n)$. The population density of $D^0(n = 2)$ is determined by a collisional-radiative model for hydrogen atom [20].

On the assumption that the quasi-steady-state solution is valid, the time derivative of eq.(1) can be set at 0. Then the set of coupled differential equations reduces to the set of coupled linear equations. The steady-state solution for the population density of C^{3+} is obtained as

$$n_{C^{3+}(p)} = R_0 n_e n_{C^{3+}} + R_1 n_e n_{C^{4+}} + R_{CX} n_{D^0} n_{C^{4+}} \qquad (2)$$

where $n_{C^{3+}}$ denotes the ground-state density of C^{3+}. Here, R_0 and R_1 are population coefficients as functions of T_e and n_e, while R_{CX} is a population coefficient as functions of T_e, n_e, and the impact energy between D^0 and C^{4+}. The first term of eq.(2) is referred to as the ionizing plasma component because it is proportional to C^{3+} density. The second term is referred to as the recombining plasma component because it is proportional to C^{4+} density. The third term is referred to as the charge exchange (CX) recombining plasma component.

Figures 5 (a) and (b) show the first, second, and third terms of eq.(2) divided by the statistical weight as a function of principal quantum number. Calculation conditions for Figs. 5 (a) and (b) are assumed to be, respectively, high temperature and low density plasma such as those of an attached divertor plasma, and low temperature and high density plasma such as those of a detached divertor plasma. In eq.(1), the different l-levels with $n \leq 5$ are treated individually, whereas the levels with $n \geq 6$, are treated as hydrogenic and assumed to be populated along the ratio of the statistical weight. As Fig. 5 (a) shows, the ionizing plasma component is dominant for the n = 7 levels in the high temperature and low density plasma. Thus, the population density of $C^{3+}(n = 7)$ can be approximated to be the ionizing plasma component. On the other hand, in the case of low temperature and high density plasma shown in Fig.5 (b), the ionizing plasma component is the largest for the $n \leq 4$ levels, and the charge exchange recombining plasma component is dominant for the $n \geq 6$ levels. Hence, the population density of $C^{3+}(n = 7)$ is approximated to be the charge exchange recombining plasma component.

3.2.2 Atomic data

Spontaneous transition probabilities $A(p, q)$ and rate coefficients for electron impact excitation/de-excitation $C(p, q)$ are taken from a data package called ADAS (Atomic Data and Analysis Structure) [21] for transitions from the $n \leq 5$ level. For transitions from the $n \geq 6$ level, $A(p, q)$ and $C(p, q)$ are calculated with a hydrogenic approximation [22].

Ionization rate coefficients $S(p)$ are calculated with the ECIP (Exchange Classical Impact Parameter) approximation [23]. Three-body recombination rate coefficients $\alpha(p)$ are inferred from the ionization rate coefficients with the principle of detailed balance, given that three-body recombination is an inverse process of ionization.

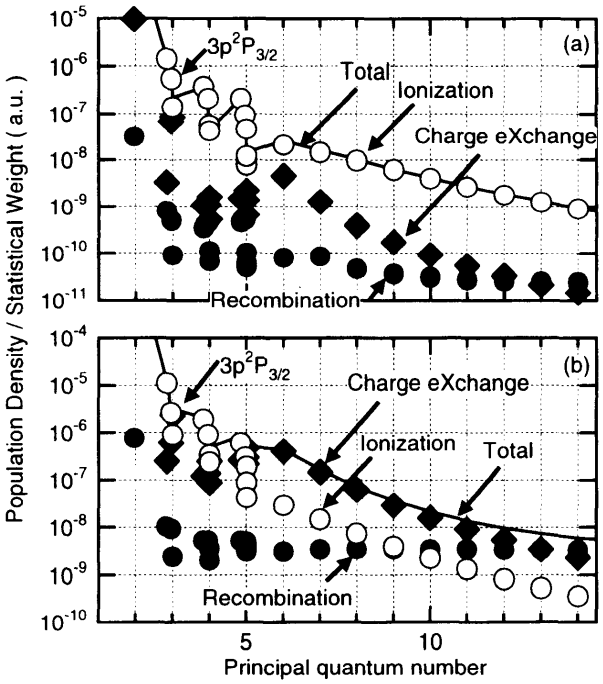

Fig. 5 Population densities of excited levels as a function of a principal quantum number. Open circles, closed circles, and closed diamonds show the ionizing, the recombining, and the charge exchange recombining plasma component, respectively. Calculation conditions are as follows :
(a) T_e = 100 eV, $T_{C^{4+}}$ = 80 eV, T_{D^0} = 30 eV, $n_e = 1.0 \times 10^{19}$ m^{-3}, $n_{D^0} = 6.0 \times 10^{16}$ m^{-3}, and $n_{C^{4+}} / n_{C^{3+}}$ = 10.
(b) n_e = 20 eV, $T_{C^{4+}}$ = 35 eV, T_{D^0} = 20 eV, $n_e = 1.7 \times 10^{20}$ m^{-3}, $n_{D^0} = 1.7 \times 10^{18}$ m^{-3}, and $n_{C^{4+}} / n_{C^{3+}}$ = 10.
Parameters of (a) attached divertor plasma and (b) detached divertor plasma are assumed.

Radiative $\beta(p)$ and di-electronic $\gamma(p)$ recombination rate coefficients are taken from the data calculated by S.N. Nahar [24] for transitions to the $n \leq 10$ level. For transitions to the $n \geq 11$ level, radiative recombination rate coefficients are calculated with a hydrogenic approximation, and di-electronic recombination rate coefficients are assumed to be equal to 0.

Rate coefficients for the charge exchange recombination $q^{CX}(n, p)$ are calculated with cross-sections taken from ADAS [21].

3.3 Estimated error of the code analysis

As shown later in Figs. 6 (a) and (b), the difference in the electron temperature and density between calculation and measurement is ~ 10%. Thus, ion temperature, calculated by the Simple Divertor code, is considered to have an error comparable to this difference. The statistical error for temperature and density of neutrals and impurities, which arises from the Monte Carlo calculation, is estimated to be ~ 5% in the divertor region. In the SOL region, however, the statistical error becomes larger (~ 10 – 20%) because the particle number is not as large as that in the divertor.In addition, uncertainty of the atomic data (typically ~ 30%) must be considered, particularly, for the population densities calculated by the collisional-radiative model. The error that

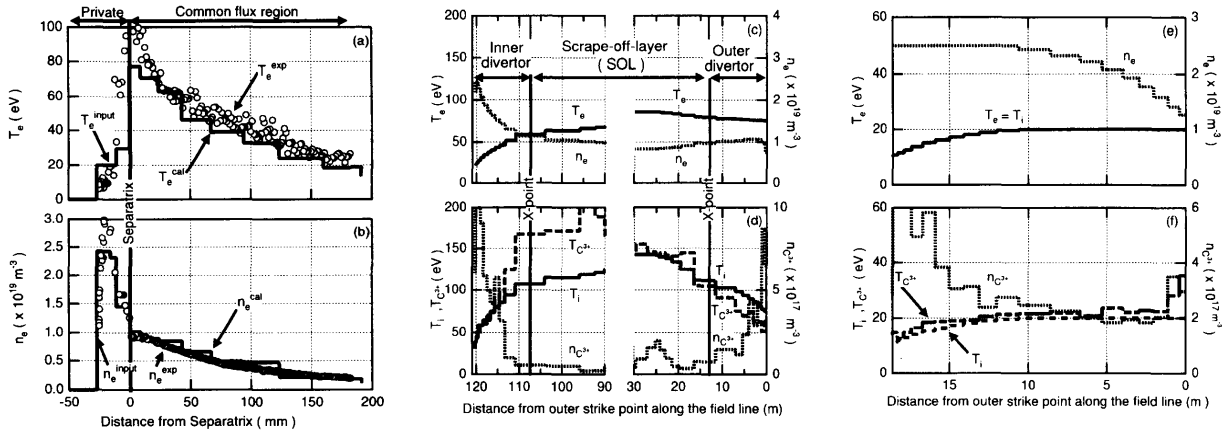

Fig. 6 (a) Electron temperature and (b) electron density measured by the reciprocating probe (T_e^{exp} and n_e^{exp}) and calculated by the Simple Divertor code (T_e^{cal} and n_e^{cal}). The electron temperature and density determined from the reciprocating probe measurement at the private region (T_e^{input} and n_e^{input}) are used as input for the IMPMC code calculation.
(c) Electron temperature (T_e), electron density (n_e), (d) ion (deuteron) temperature (T_i), C^{3+} temperature ($T_{C^{3+}}$), and C^{3+} density ($n_{C^{3+}}$) along the flux tube closest to the separatrix in the common flux region. The electron temperature, the electron density, and the ion temperature were calculated by the Simple Divertor code, and the C^{3+} temperature and density by the IMPMC code.
(e) Electron temperature, electron density, (f) ion (deuteron) temperature, C^{3+} temperature, and C^{3+} density along the flux tube in a private region. The electron temperature, the electron density, and the ion temperature were assumption based on the electron temperature and density measured by the reciprocating probe at ~ 10 m from the outer divertor plates. The C^{3+} temperature and density were calculated by the IMPMC code.

arises from the assumption that l-levels of $n \geq 6$ are treated as hydrogenic and populated along the statistical population-distribution is less than ~ 20% [25]. In the present work, this error can be neglected based on the fact that the population-distribution of l-levels of $n = 6$ and 7 is found to be close to the ratio of the statistical weight, as described above.

4. Results

In Figs. 6 (a) and (b), respectively, the electron temperature and density along the reciprocating probe chord are shown. For the common flux region, both the electron temperature and density calculated by the Simple Divertor code are in reasonable agreement with those measured. This result does not only confirm the validity of the calculated electron temperature and density but also supports the separatrix location. This result supports that the cold and dense plasma observed near the separatrix is located in the private region. This density peak in the private region was also observed in ASDEX-Upgrade [26] and DIII-D [27]. In JT-60U, it was found to appear and disappear with the ion $\nabla \mathbf{B}$ drift-direction downward and upward, respectively [28].

Figure 6 (c) shows electron temperature and density, and Figure 6 (d) shows bulk ion (deuteron, D^+) temperature, C^{3+} temperature, and C^{3+} density along the flux tube closest to the separatrix as a function of field line length from the outer divertor plate to the inner divertor plate. The outer divertor plasma is hot and is not dense, resulting in almost constant electron temperature and density along the flux tube. In such a plasma, the temperature relaxation time between C^{3+} and D^+ is too long for D^+ to heat C^{3+} up to the D^+ temperature. Thus, in the region from 0 m to 13 m, the C^{3+} temperature is lower than the D^+ temperature. In the SOL plasma, for reasons similar to those for the outer divertor plasma, the C^{3+} temperature is not equal to the D^+ temperature. However, because C^{3+} transported from the core plasma, whose temperature is higher than the D^+ temperature, is dominant, the C^{3+} temperature is higher than the D^+ temperature. In contrast to the outer divertor and the SOL plasma, the inner divertor plasma is so cold and dense that the gradients of the electron temperature and density are generated. In particular, at the plasma close to the inner divertor plates, the region from 115 m to 120 m, the C^{3+} temperature is close to the D^+ temperature because the relaxation time between C^{3+} and D^+ is sufficiently short.

Figures 6 (e) and (f) show parameters similar to those shown in Figs. 6 (c) and (d), respectively, along a flux tube of the private region. The electron temperature and density between the inner and the outer divertor plates are assumed as shown in Fig. 6 (e) in consideration of the electron temperature and density measured by the reciprocating probe shown in Figs. 6 (a) and (b). The D^+ temperature is assumed to be equal to the electron temperature. The result from the IMPMC code indicates that the C^{3+} temperature is close to the D^+ temperature as Fig. 6 (f) shows.

Figure 7 shows measured C^{3+} temperature, calculated C^{3+} temperature, and D^+ temperature as a function of spectroscopic viewing chord number. As already described, two C^{3+} temperatures were inferred from the observed C IV ($n = 6 - 7$) spectral line. The higher C^{3+} temperature, $T_{C^{3+}}^{exp}$(High), is in the range from 50 eV to 150 eV, the lower, $T_{C^{3+}}^{exp}$(Low), around 20 eV. The calculated C^{3+} temperature and D^+ temperature were weight-averaged along a viewing chord.

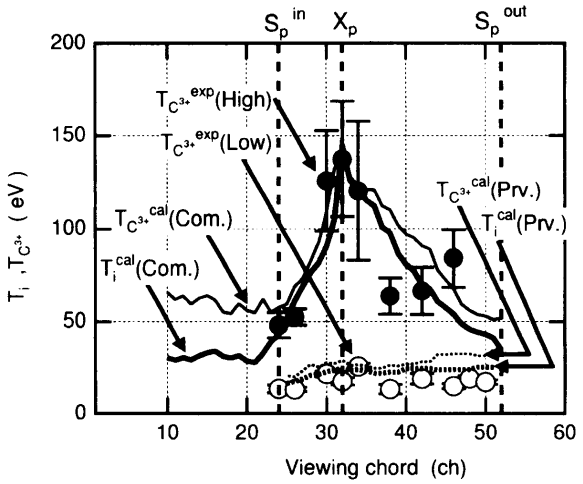

Fig. 7 Comparison of measured C^{3+} temperature, calculated C^{3+} temperature, and D^+ temperature. $T_{C^{3+}}^{exp}$(High) and $T_{C^{3+}}^{exp}$(Low) indicate the measured C^{3+} temperature of the high and the low temperature component, respectively. $T_{C^{3+}}^{cal}$(Com) and $T_{C^{3+}}^{cal}$(Prv) (T_i^{cal}(Com) and T_i^{cal}(Prv)) indicate the calculated C^{3+}(D^+) temperatures of the common flux region and of the private region, respectively. S_p^{in}, X_p, and S_p^{out} indicate the inner strike point, the X-point, and the outer strike point, respectively.

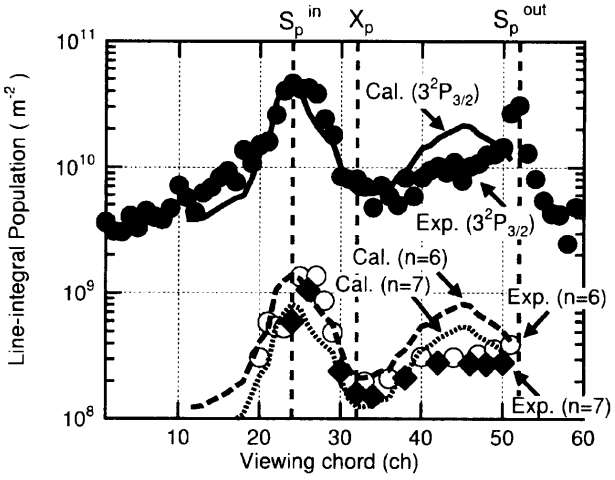

Fig. 8 Comparison of measured and calculated line-integral population densities. Closed circles, open circles, and closed diamonds show the measured line-integral population densities of $C^{3+}(3p^2P_{3/2})$, $C^{3+}(n = 6)$, and $C^{3+}(n = 7)$, respectively. Solid, dashed, and dotted lines show the calculated line-integral population densities of $C^{3+}(3p^2P_{3/2})$, $C^{3+}(n = 6)$, and $C^{3+}(n = 7)$, respectively.

Here, the intensity of the C IV ($n = 6 - 7$) spectral line was used as the weight. Because the temperature of the common flux plasma was substantially different from that of the private plasma, the weight-average operation was performed separately for the common flux plasma and for the private plasma. Thus, two calculated C^{3+} temperatures are shown in Fig. 7: $T_{C^{3+}}^{cal}$(Com) for the common flux plasma and $T_{C^{3+}}^{cal}$(Prv) for the private plasma. Similarly, two D^+ temperatures, T_i^{cal}(Com) and T_i^{cal}(Prv), are shown. As the figure shows, comparison of measured and calculated C^{3+} temperatures suggests that $T_{C^{3+}}^{exp}$(High) and $T_{C^{3+}}^{exp}$(Low) correspond to $T_{C^{3+}}^{cal}$(Com) and $T_{C^{3+}}^{cal}$(Prv), respectively. In the inner divertor, $T_{C^{3+}}^{cal}$(Com) and $T_{C^{3+}}^{cal}$(Prv) are in agreement with T_i^{cal}(Com) and T_i^{cal}(Prv). But this agreement is not obtained in the outer divertor. The reason is discussed in the next section.

Figure 8 shows the line-integral population densities of $C^{3+}(3p^2P_{3/2})$, $C^{3+}(n = 6)$, and $C^{3+}(n = 7)$. The measured and calculated line-integral population density of $C^{3+}(n = 7)$ includes, respectively, those of both the high and the low temperature component, and those of both the common flux plasma and the private plasma. The measured line-integral population densities are in reasonable agreement with the calculated ones, excepting those around 45 ch. Around 45 ch, there is a factor of ~ 2 difference between the measurement and the calculation. Given that about 90% of the $C^{3+}(n = 7)$ population density is the ionizing plasma component, which is proportional to the ground-state C^{3+} density, this difference is ascribed to overestimation of the ground-state C^{3+} density in the impurity transport calculation by the IMPMC code. The peak of the $C^{3+}(3p^2P_{3/2})$ population density around 52 ch, which views the outer divertor plates, is considered to be due to emission from D_2 molecules. Because the brightness of the C IV ($3s^2S_{1/2} - 3p^2P_{3/2}$) spectral line was measured by the interference filter optics, continuum lines such as molecular emission were included simultaneously.

From the above analyses, the spectrum summed along a viewing chord was calculated. Figure 2 shows comparison of the measured and the calculated spectrum of C IV ($n = 6 - 7$) along the viewing chord 34 ch, which views the X-point. The measured spectrum is in reasonable agreement with the calculated spectrum. This agreement results from agreement of both the temperature and the population density. In more detail, $T_{C^{3+}}^{exp}$(High) and $T_{C^{3+}}^{exp}$(Low) agree with $T_{C^{3+}}^{cal}$(Com) and $T_{C^{3+}}^{cal}$(Prv), respectively, and a similar correspondence holds for the population density: $n_{C^{3+}}^{exp}$(High) and $n_{C^{3+}}^{exp}$(Low) agree with $n_{C^{3+}}^{cal}$(Com) and $n_{C^{3+}}^{cal}$(Prv), respectively. The slight difference around the tails of the spectrum is due to overestimation of $T_{C^{3+}}^{cal}$(Com).

5. Discussion

In order to measure the D^+ temperature from the Doppler broadening of the C IV spectral line, the following conditions have to be satisfied; the ionization time ($\tau_{C^{3+}}^{ioniz}$) and the parallel transport time ($\tau_{C^{3+}}^{trans//}$) of C^{3+} have to be longer than the temperature relaxation time between C^{3+} and D^+($\tau_{C^{3+},i}^{relax}$). Here, $\tau_{C^{3+}}^{trans//}$ is calculated from a thermal velocity of C^{3+}. In the present study, because $\tau_{C^{3+}}^{ioniz}$ is longer (> 100 μs) than $\tau_{C^{3+}}^{trans//}$ in most cases, the time scale of $\tau_{C^{3+}}^{trans//}$ and $\tau_{C^{3+},i}^{relax}$, is compared.

In Fig. 9 (a), the C^{3+} temperature and the D^+ temperature determined by the transport codes are shown as a function of distance along the viewing chord 25 ch. In most cells, the C^{3+} temperature is close to the D^+ temperature. This agreement is explained in terms of the time scale of $\tau_{C^{3+},i}^{trans//}$

and $\tau^{relax}_{C^{3+},i}$. As Figure 9 (b) shows, $\tau^{relax}_{C^{3+},i}$ is shorter than or comparable to $\tau^{trans//}_{C^{3+},i}$. The temperature relaxation between C^{3+} and D^+ occurs in most cells. As a result, the agreement between the weight-averaged C^{3+} temperature and the weight-averaged D^+ temperature is obtained, as already shown in Fig. 7. The weight-averaged C^{3+} temperature is affected most by the C^{3+} temperature at the divertor leg, because the population density of $C^{3+}(n = 7)$ at the cell closest to the divertor leg is dominant, as shown in Fig. 9 (a). This is the case for the viewing chords between 24 ch and 32 ch, which view the inner divertor plasma. Therefore, it is concluded that the D^+ temperature around the inner divertor leg can be measured by the C IV ($n = 6 - 7$) spectral line.

In the outer divertor, on the other hand, it can be understood from similar discussion that the D^+ temperature cannot be measured by the C IV spectral line; as shown in Fig. 9 (c), the C^{3+} temperature differs from the D^+ temperature in all the cells. This difference is ascribed to insufficient temperature relaxation due to longer $\tau^{relax}_{C^{3+},i}$ than $\tau^{trans//}_{C^{3+},i}$. This is the reason the weight-averaged C^{3+} temperature is different from the weight-averaged D^+ temperature shown in Fig. 7. As Figure 9 (c) shows, the population density of $C^{3+}(n = 7)$ is the largest at the cell around the divertor leg. Notably, the contribution from the other cells, corresponding to the divertor region as well as the SOL region, to the line-integral population density is also significant. This widespread distribution of the emission zone is one of the reasons it is difficult to predict the position of the plasma whose temperature is measured by the C IV spectral line.

Discussion of a problem that arose from the assumption of the plasma parameters in the private plasma is given. As can be understood from Fig. 2, the agreement between the measured $C^{3+}(n = 7)$ population density of the low temperature component, $n^{exp}_{C^{3+}(n=7)}$(Low), and the calculated one in the private plasma, $n^{cal}_{C^{3+}(n=7)}$(Prv), was obtained along the viewing chord 34 ch. This agreement results from appropriate plasma parameters, T_e, n_e, and T_i, which were determined from the reciprocating probe measurement. However, the agreement between $n^{exp}_{C^{3+}(n=7)}$(Low) and $n^{cal}_{C^{3+}(n=7)}$(Prv) becomes worse along the viewing chords away from the 34 ch. In most of the viewing chords, $n^{exp}_{C^{3+}(n=7)}$(Low) is larger than $n^{cal}_{C^{3+}(n=7)}$(Prv). This underestimation of $n^{cal}_{C^{3+}(n=7)}$(Prv) is ascribed mainly to inappropriate input of the plasma parameters, in particular n_e. Because diffusion and radial drifts across the separatrix to the private region are considered to determine the plasma parameters, it is difficult to assume appropriate T_e, n_e and T_i in all the cells.It is expected that a two-dimensional transport code such as SONIC [29] or spatial resolution measurement such as Thomson scattering [27] could help to solve this problem.

The above results and discussion have been described for the attached divertor plasma. For detached plasmas, since the Simple Divertor code cannot determine the plasma parameters, T_e and n_e measured by the reciprocating probe (T_e = 20 eV, $n_e = 1.7 \times 10^{20}$ m^{-3}) were used for the analysis of the collisional-radiative model. As shown in Fig. 5 (b), the calculated ratio of the population density of $C^{3+}(n = 7)$ to $C^{3+}(3p^2P_{3/2})$ is about 0.1. This ratio is in good agreement with the ratio measured in the detached plasma. This agreement

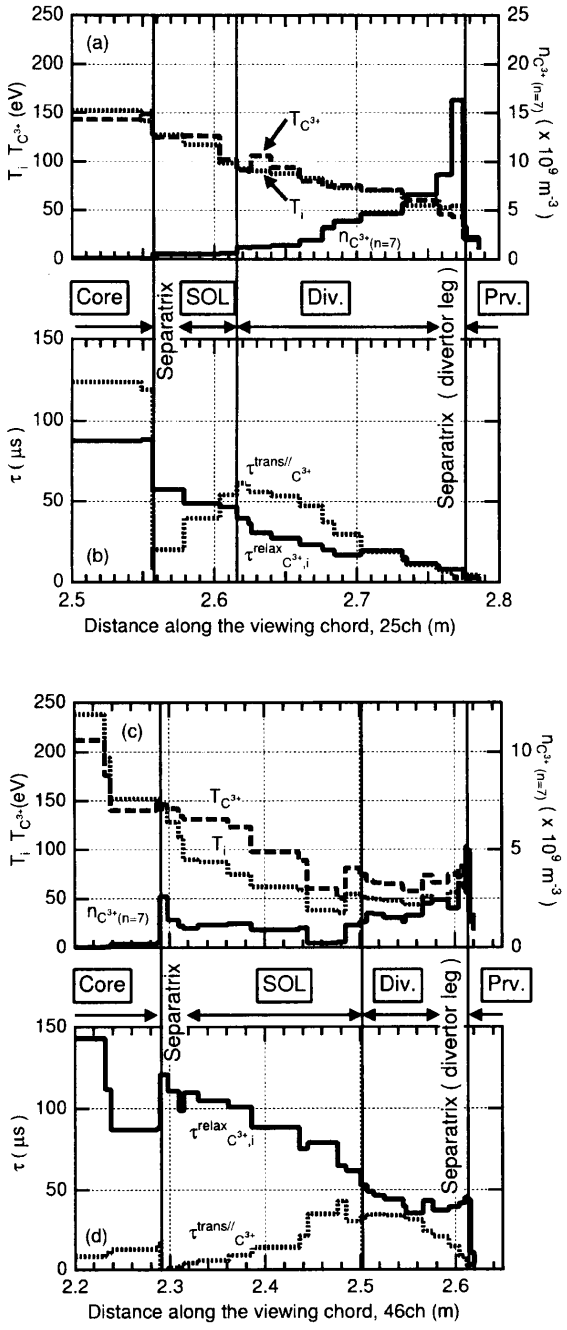

Fig. 9 (a) C^{3+} temperature (dashed line) , D^+ temperature (dotted line), population density of $C^{3+}(n = 7)$ (solid line), (b) temperature relaxation time ($\tau^{relax}_{C^{3+},i}$) between C^{3+} and D^+ (solid line), and parallel transport time ($\tau^{trans//}_{C^{3+}}$) (dotted line) along the viewing chord 25ch. The distance is measured from the focal point on the edge of the optical fiber array at the upper side of the vacuum vessel shown in Fig. 1 (a). The viewing chord penetrates the core plasma (denoted by 'Core'), the SOL plasma ('SOL'), the divertor plasma ('Div.'), and the private plasma ('Prv.') before it reaches the divertor structure. Comparison similar to (a) and (b) is shown in (c) and (d) for 46 ch, respectively.

suggests that the charge exchange recombination from $D^0(n = 2)$ to C^{4+} is a dominant process to populate the $n = 7$ level of C^{3+}. Thus, the temperature inferred from the C IV ($n = 6 - 7$) spectral line reflects the C^{4+} temperature. Given that the temperature relaxation time of deuteron with carbon ion is inversely proportional to the square of the carbon ion charge, the temperature relaxation time with C^{4+} is shorter than that with C^{3+}. Therefore, detached plasmas are preferred for the ion temperature measurement using the C IV ($n = 6 - 7$) spectral line. This result also indicates that the neutral deuterium penetrates more deeply in detached plasmas than in attached plasmas. The charge exchange recombination process becomes dominant in cases in which a large amount of neutral deuterium, for example, 1% of n_e, as shown in Fig. 5, reaches relatively hot plasmas in which C^{4+} exists. This situation was not observed in the attached plasma analyzed above. Neutral deuterium generated by recombination between e^- and D^+ as well as that recycled from the divertor plates is believed to play a role in the longer penetration depth.

6. Conclusions

We have investigated the spatial distribution of C^{3+} temperature and C^{3+} density in divertor plasmas in order to understand the transport of carbon ions, aiming particularly at ion (deuteron) temperature measurement. Simultaneous measurement of three spectral lines, C IV ($3s^2S_{1/2} - 3p^2P_{3/2}$), C IV ($n = 5 - 6$), and C IV ($n = 6 - 7$), provided the population densities, $C^{3+}(3p^2P_{3/2})$, $C^{3+}(n = 6)$, and $C^{3+}(n = 7)$, respectively, whose ratio reveals the excitation processes of C^{3+}. From the results of analyses using two-dimensional transport codes [4,17] and a collisional-radiative model, it is concluded that $C^{3+}(n = 7)$ is predominantly excited from the ground-state of C^{3+} by electron collision in all the regions of the divertor plasma under the attached condition. Hence, it is found that the temperature inferred from the Doppler broadening of the C IV ($n = 6 - 7$) spectral line reflects C^{3+} temperature, and that C^{3+} density can be measured from the brightness of the spectral line.

A high wavelength resolution spectrometer [10] enabled us to measure a detailed profile of the C IV ($n = 6 - 7$) spectral line. Regression analysis of the spectrum resulted in two C^{3+} temperature components. The higher C^{3+} temperature ranged from 50 eV to 150 eV, the lower around 20 eV. From the results of the code analyses, it is concluded that the higher and the lower C^{3+} temperature correspond to the C^{3+} temperature of the common flux plasma and of the private plasma, respectively. Further, the code analyses indicate that C^{3+} temperature is close to D^+ temperature in the inner divertor, and that the C IV spectral line is predominantly emitted around the inner divertor leg. Therefore, it is concluded that D^+ temperature around the inner divertor leg can be measured from the C IV spectral line. In contrast, in the outer divertor, similar analyses indicate that it is difficult to measured the D^+ temperature.

In the private plasma, the code analyses underestimated the population density of $C^{3+}(n = 7)$ except for that below the X-point. This is due to difficulty in estimating the plasma parameters. The private plasma is often regarded as trivial, and has not been allocated sufficient attention. However, it is reported that a significant number of particles flow through the private region from the outer to the inner divertor [30]. This particle flux might explain the asymmetry between the inner and the outer divertor plasma. Further studies on the private plasma are required to understand the transport of the divertor plasmas.

In detached plasmas, comparison of the population densities between measurement and calculation indicates that $C^{3+}(n = 7)$ is predominantly populated by the charge exchange recombination between $D^0(n = 2)$ and C^{4+}. In this case, the temperature inferred from the Doppler broadening of the C IV ($n = 6 - 7$) spectral line reflects the C^{4+} temperature. Because the C^{4+} temperature tends to be closer to the D^+ temperature than the C^{3+} temperature is in terms of the temperature relaxation time, the detached plasma is preferred to the attached plasma for the purpose of ion temperature measurement. The result also indicates that the neutral deuterium can penetrate deeply enough to reach C^{4+}. The neutral deuterium behaviors in detached JT-60U divertor plasmas have not yet been investigated by transport codes. We are planning to conduct such investigation using a transport code called SONIC [29], which can calculate the two-dimensional distribution of plasma parameters in detached plasmas.

Finally, it should be noted in terms of atomic physics that the wavelength of the C IV ($n = 6 - 7$) spectral lines have been determined with significantly improved accuracy. The agreement between experimentally-determined wavelength and calculated wavelength [13] has been improved significantly. Comparison of the wavelength with high accuracy contributes to an understanding of the atomic structure such as energy levels.

Acknowledgments

The authors would like to acknowledge Dr. N. Nahar of Ohio State Univ. for providing the recombination rate coefficients in a tabulated form, and Dr. T. Kawachi of Japan Atomic Energy Research Institute and Dr. K. Sawada of Shinshu Univ. for providing the collisional-radiative model for lithium-like ions and hydrogen, respectively. Helpful maintenance of the diagnostics by S. Nagaya, M. Onizawa, and M. Nakata, modification of the transport codes by Mr. I. Kamata, fruitful discussions with Dr. M. Shimada and Dr. Y. Kawano, and continuous support by Dr. Y. Miura are greatly appreciated.

References

[1] N. Asakura, S. Sakurai *et al.*, Phys. Rev. Lett. **84**, 3093 (2000).

[2] R.K. Janev, Yu. V. Ralchenko *et al.*, *NIFS-DATA-62*, National Institute for Fusion Science (2001).

[3] T. Nakano, H. Kubo *et al.*, Nucl. Fusion **42**, 689 (2002).

[4] K. Shimizu, H. Kubo *et al.*, J. Nucl. Mater. **220-222**, 410 (1995).
[5] H. Kubo, H. Takenaga *et al.*, Plasma Phys. Control. Fusion **41**, 747 (1999).
[6] M.J. Schaffer, J.A. Boedo *et al.*, J. Nucl. Mater. **290-293**, 530 (2001).
[7] I. Katsumata, Contrib. Plasma Phys. **36S**, 73 (1996).
[8] N. Ezumi, S. Masuzaki *et al.*, J. Nucl. Mater. **313-316**, 696 (2003).
[9] A. Huber, A. Pospieszczyk, B. Unterberg *et al.*, Plasma Phys. Control. Fusion **42**, 569 (2000).
[10] H. Kubo, T. Sugie *et al.*, Fusion Eng. Des. **34/35**, 277 (1997).
[11] L. Minnhagen, J. Opt. Soc. Am **63**, 1185 (1973).
[12[S. Bashkin and J.O. Stoner, Jr., *Atomic Energy Levels and Grotrian Diagrams 1* (North-Holland, Amsterdam, 1975).
[13] P. Quinet, Astron. Astrophys. Suppl. Ser. **129**, 603 (1998).
[14] T. Nakano, H. Kubo *et al.*, *JAERI-Review*, Japan Atomic Energy Research Institute **2000-5**, 151 (2002).
[15] H. Kubo, T. Sugie *et al.*, Plasma Phys. Control. Fusion **37**, 1133 (1995).
[16] N. Asakura, S. Tsuji-Iio *et al.*, Rev. Sci. Instrum. **66**, 5428 (1995).
[17] K. Shimizu, K. Itami *et al.*, J. Nucl. Mater. **196-198**, 476 (1992).
[18] C.F. Maggi, L.D. Horton and H.P. Summers, Plasma Phys. Control. Fusion **42**, 669 (2000).
[19] M.G. O'Mullane, M. Mattioli *et al.*, Plasma Phys. Control. Fusion **41**, 105 (1999).
[20] K. Sawada and T. Fujimoto, J. Appl. Phys. **78**, 2913 (1995).
[21] H.P. Summers, *JET-IR* 06 (1994), http://adas.phys.strath.ac.uk/
[22] A. Burgess and H.P. Summers, Mon. Not. R. Astr. Soc. **174**, 345 (1976).
[23] A. Burgess, Astrophys. J. **139**, 776 (1964).
[24] S.N. Nahar, A.K. Pradhan and H.L. Zhang, Astrophys. J. Suppl. Series. **131**, 375 (2000).
[25] T. Kawachi, T. Fujimoto and G. Csanak, Phys. Rev. E **51**, 1428 (1995).
[26] H.-S. Bosch, J. Neuhauser *et al.*, J. Nucl. Mater. **220-222**, 558 (1995).
[27] J.G. Watkins, J. Hunter *et al.*, Rev. Sci. Instrum. **68**, 373 (1997).
[28] S. Sakurai, N. Asakura *et al.*, J. Nucl. Mater. **266-269**, 1191 (1999).
[29] K. Shimizu, T. Takizuka *et al.*, J. Nucl. Mater. **313-316**, 1277 (2003).
[30] N. Asakura, S. Sakurai *et al.*, J. Nucl. Mater. **313-316**, 820 (2003).